ORIGINAL PAPER

Effect of Ce^{3+} Ion on Structural and Hyperfine Interaction Studies of $Co_{0.5}Ni_{0.5}Fe_{2-x}Ce_xO_4$ Ferrites: Useful for Permanent Magnet Applications

K. M. Srinivasamurthy[1] · V. Jagadeesha Angadi[2] · S. P. Kubrin[3] · Shiddaling Matteppanavar[4] · D. A. Sarychev[3] · B. Rudraswamy[1]

Abstract

Nanoparticles of $Co_{0.5}Ni_{0.5}Fe_{2-x}Ce_xO_4$ (where $x = 0.0, 0.01, 0.015$ and 0.02) ferrites are prepared by the modified solution combustion method using a mixture of fuels and are characterized to understand their structural, microstructural and magnetic properties. The X-ray diffraction is used to confirm the formation of a single-phase cubic spinel structure. The average crystallite sizes are calculated using the Scherrer formula and are found to be less than 50 nm. The microstructural features are obtained by the scanning electron microscopy, and the compositional analysis is done by using the energy-dispersive spectroscopy. The transmission electron microscopy (TEM) investigations show that the synthesized ferrites are made up of very fine spherical nanoparticles. The influence of a rare-earth element (Ce^{3+}) on the magnetic properties of the samples was studied using the Mössbauer spectroscopy. The Mössbauer spectroscopy reveals the formation of broadened Zeeman lines and quadrupole-split lines and the presence of the Fe^{3+} charge state at B sites in the samples. The quadrupole splitting shows that the orientation of the magnetic hyperfine field with respect to the principle axes of the electric field gradient was random. The magnetic hyperfine field values indicate that the A sites have more A-O-B superexchange interactions than the B sites. The coexistence of magnetic sextet and a doublet component on the room-temperature spectra suggests superparamagnetic properties of the nanoparticles. The low-temperature (15 K) Mössbauer spectroscopy explores the paramagnetic relaxation in the nanoparticles. The area under the sextet refers to Fe^{3+} concentrations in the tetrahedral and octahedral sites of the ferrite. This study confirms that the Ce^{3+} substitution of Fe^{3+} only for octahedron sites causes the decrease in Fe-O-Fe arrangement. The effect of Ce^{3+} doping on the magnetic properties of $Co_{0.5}Ni_{0.5}Fe_2O_4$ is examined from the vibrating sample magnetometry (VSM) spectra. Saturation magnetization values are decreased initially and then increased, as result of Ce^{3+} doping. This can be explained by Neel's two-sub-lattice model. Further, the value of coercivity is found to be increasing with increasing Ce^{3+} concentration. The obtained results of M-H loop with improved coercivity (from 851 to 1039 Oe) by Ce^{3+} doping of $Co_{0.5}Ni_{0.5}Fe_2O_4$ demonstrate the usefulness for permanent magnet applications.

Keywords Rietveld refinement · Mossbauer spectroscopy · Superparamagnetic relaxation · Nanoparticles

✉ V. Jagadeesha Angadi
jagadeeshaangadi@presidencyuniversity.in

[1] Department of Physics, Bangalore University, Bangalore, 560056, India

[2] Department of Physics, School of Engineering, Presidency University, Bangalore, 560064, India

[3] Research Institute of Physics, Southern Federal University, Rostov-on-Don, Russia

[4] Department of Physics, M. S. Ramaiah University of Applied Sciences, Bangalore, 560058, India

1 Introduction

Over the recent years, researchers have been trying to modify the properties of spinel ferrites by the substitution of various divalent and trivalent metal ions in the ferrite system [1–4]. Doping a spinel ferrite structure by rare-earth ions is increasingly important because of the growing number of applications compared to similar ferrite systems [5–8]. Due to high permeability, saturation magnetization and low coercivity, rare-earth-doped ferrites are promising candidates for numerous microwave applications, such as circulators, phase shifters, isolators, power

transformations, memory core devices, antennas and high-speed digital tapes, high-density data storage devices, catalysts, magnetic liquids and microwave absorbers [9–11]. As a token of interest, we consider the rare-earth-doped Co-Ni mixed ferrite system to obtain new results relevant for technological applications [12]. The Lanthanum series (rare-earth elements: La, Sm, Gd, Dy, Yb, Er, Tb, Ce and Y)-doped ferrites show significant perturbations in structural distortions and electrical and magnetic properties [13–16]. Incorporation of rare-earth ions at Fe^{3+} site decreases the Fe-O-Fe interactions, and the occurrence of simultaneous Re-Fe interactions leads to the enhancement of magnetic properties in the ferrites [17–22]. In the present investigation, we introduce larger-ionic radius Ce^{3+} at the Fe^{3+} site of $Co_{0.5}$-$Ni_{0.5}$ ferrites. For the first time, we have synthesized the ferrite samples by the modified solution combustion method using a mixture of carbamide and urea as fuels and have reported the influence of Ce^{3+} on the structural, microstructural, magnetic and low-temperature Mössbauer spectroscopic properties and room-temperature field-dependent magnetic properties of $Co_{0.5}Ni_{0.5}Ce_xFe_{2-x}O_4$ (where $x = 0.0$, 0.01, 0.015 and 0.02). The results of the present work suggest that the synthesized material can be nominated candidates for permanent magnet applications.

2 Experimental

2.1 Precursors

All the materials were 99% pure AR grade cobaltous nitrate hexahydrate $[Co(NO_3)_2 \cdot 6H_2O]$, nickel nitrate hexahydrate $[Ni(NO_3)_2 \cdot 6H_2O]$, ferrous nitrate nanohydrate $[Fe(NO_3)_3 \cdot 9H_2O]$ and cerium nitrate hexahydrate $[Ce(NO_3)_3 \cdot 6H_2O]$ as oxidizers, while carbamide and glucose as a mixture of fuels. The water was distilled twice to avoid impurities.

2.2 Synthesis

For the synthesis of $Co_{0.5}Ni_{0.5}Fe_{2-x}Ce_xO_4$ (where $x = 0.0$, 0.01, 0.015 and 0.02), stoichiometric amounts of oxidizer and fuel are taken in the ratio 1:1 (O/F = 1), dissolved in a 500-ml capacity Pyrex glass beaker and diluted with 50 ml double-distilled water, then are thoroughly mixed by a magnetic stirrer at 800 rpm for about 40 min until all the precursors dissolve completely to obtain a homogeneous clear solution. This clear solution is kept into a preheated muffle furnace at 450 ± 10 °C. Initially, the solution boils and then undergoes dehydration, and the voluminous gases of nitrogen, carbon dioxide and water vapour are released. The left-out mass gets ignited, resulting in a very soft

product. This resultant product is ground in an agate mortar to get a fine powder for further use.

2.3 Methods

The obtained fine powdered sample is characterized by X-ray diffraction (XRD) using a PANanalytical X-ray diffractogram with a CuK_α radiation of wavelength 1.542 Å in the 2θ value ranging from 20° to 80° with a step size of 0.02°. Rietveld refinements for the obtained XRD patterns are carried out using Fullproof software. The scanning electron microscopy (SEM) and energy-dispersive spectroscopy (EDS) spectra are collected using JEOL (model JSM-840) to investigate the morphology and elemental analysis of the samples. Transmission electron microscopy (TEM) and selected area electron diffraction (SAED) are performed using Philips (model CM 200) to estimate the particle size of the samples to confirm the crystallinity of the samples. The Mössbauer spectra are obtained using the MS1104Em Mössbauer spectrometer. The ^{57}Co in Rh matrix is used as a γ-ray source. The samples are cooled in helium cryostat CCS-850 (Janis Res., Inc., USA). The Mössbauer experimental spectra are fitted using SpectrRelax software. The magnetic properties of all the samples explored using Lakeshore 7410 vibrating sample magnetometer (VSM) with a maximum applied field of 20 kOe.

3 Results and Discussion

3.1 Structural Analysis

Rietveld refined X-ray diffraction patterns of $Co_{0.5}Ni_{0.5}Fe_{2-x}Ce_xO_4$ (where $x = 0.0$, 0.01, 0.015 and 0.02) nanoparticles are shown in Fig. 1. The XRD data for the samples with $x = 0.0$ composition are given in ref. [26] and also presented here for comparison. All the samples have cubic inverse spinel structure. All the XRD peaks are indexed, the *hkl* plane of the peaks refers to *Fd3m* space group and the nonoccurrence of extra peak in the XRD pattern suggests the synthesized sample-phase purity. The major intense peaks of the XRD pattern are indexed as (220), (311), (222), (400), (422), (511) and (440), and all the peaks match well with the characteristic reflections. The fitting of all the peaks is carried out using GSAS program. In addition to a low value of χ^2, the residue factors, i.e. Rp and Rwp, are less than 0.1, which indicates a good agreement of the observed patterns with the calculated ones. The crystallite size (D_{hkl}) is calculated by using the Debye-Scherrer formula [23]

$$D_{hkl} = \frac{k\lambda}{\beta \cos \theta} \tag{1}$$

Fig. 1 Rietveld refined XRD patterns of $Co_{0.5}Ni_{0.5}Fe_{2-x}Ce_xO_4$ (where $x = 0.0, 0.01, 0.015$ and 0.02)
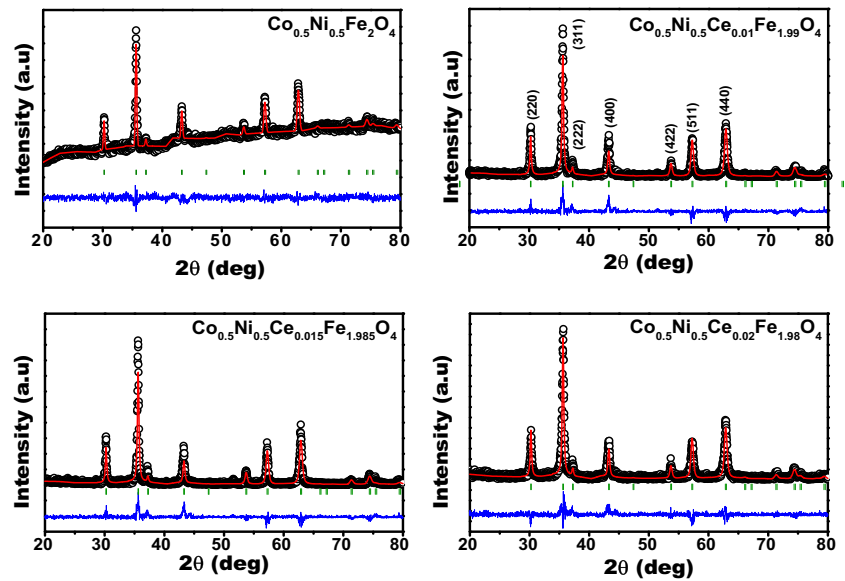
where k is Bragg's constant, β is the FWHM in radians, λ is the wavelength of X-ray and θ is Bragg's diffraction angle. The average crystallite size of the samples is presented in Table 1. The lattice parameter a of the samples is estimated using the formula [24]

$$a = d_{hkl}\sqrt{(h^2 + k^2 + l^2)} \qquad (2)$$

$$d_{hkl} = \frac{\lambda}{\beta \sin\theta} \qquad (3)$$

where d_{hkl} is the interplanar spacing and (hkl) is miller indices. The influence of larger-ionic radius Ce^{3+} (1.14 Å) at the site of Fe^{3+} (0.63 Å) in a spinel ferrite decreases the lattice parameter from 8.313 to 8.245 Å with the growth of a dopant concentration. This is due to lattice distortion which leads to lesser arrangement of $Ce^{3+}-O^{2-}$ bonds. This induces a larger crystalline anisotropy and develops internal strains inside the lattice volume with an increasing Ce^{3+} concentration. In order to balance the crystalline anisotropy and internal strain, the crystallite size decreases. The Fe^{3+} ions in spinel ferrites can occupy both tetrahedral and octahedral sites. The introduced Ce^{3+} ions have the tendency to occupy the octahedral sites. Yet, it is difficult for Ce^{3+} to substitute Fe^{3+} because of its ionic radii being larger than those of Fe^{3+}. These need larger activation energy to enter the octahedral sites, which leads to a decrease in crystallite size and lattice parameter. In addition, the average crystallite size (D_{W-H}) and internal strains (ε) of the samples are determined by the Williamson-Hall relation [25]

$$\beta \cos\theta = \frac{k\lambda}{D_{W-H}} + 4\varepsilon\sin\theta \qquad (4)$$

where β is the FWHM of the diffraction peaks in radians. A plot of ($\beta\cos\theta$) along the Y-axis and ($4\sin\theta$) along the X-axis for every sample under investigation is presented in Fig. 2. From the linear fit of the data, the slope of the line indicates the lattice strain induced in the samples, and the intercept on the Y-axis shows the effective crystallite size. The lattice strain (ε) and effective crystallite size (D_{W-H}) in nanometres determined from Williamson-Hall plots are listed in Table 1. From the W-H plots, it is clear

Table 1 Crystallite size, lattice parameter, X-ray density, crystallite size and internal strain from the W-H plot as well as particle size from TEM of $Co_{0.5}Ni_{0.5}Fe_{2-x}Ce_xO_4$ ferrites where $x = 0.0, 0.01, 0.015$ and 0.02

Ce^{3+} concentration (x)	Crystallite size (D_{hkl}, nm)	Lattice parameter (a, Å)	χ^2	X-ray density (Δ, g/cm³)	Particle size from TEM (nm)	W-H plot	
						Crystallite size (D_{W-H}, nm)	Internal strain ($\times 10^4$)
0.00	35.157	8.36254	1.37	5.326	50	35.5	27.1
0.01	27.288	8.35876	1.56	5.353	30	33.3	29.5
0.015	26.598	8.35844	1.90	5.363	29	31.9	35.5
0.02	25.888	8.35805	1.48	5.371	28	30.6	37.3

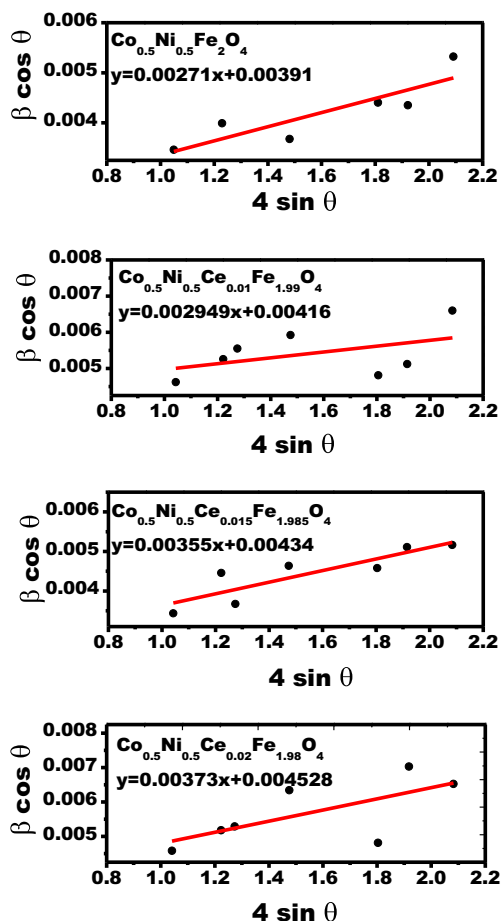**Fig. 2** Williamson-Hall plots of $Co_{0.5}Ni_{0.5}Fe_{2-x}Ce_xO_4$ (where $x = 0.0, 0.01, 0.015$ and 0.02)

that the replacement of Fe^{3+} by Ce^{3+} in the $Co_{0.5}Ni_{0.5}$ ferrites perturbs appreciably the crystallite size and lattice strain in the samples. The variation in the crystallite size estimated from XRD using the Debye-Scherrer formula and Williamson-Hall relation is consistent with each other. The trend of crystallite size from the Scherrer formula and W-H plots is shown in Fig. 3.
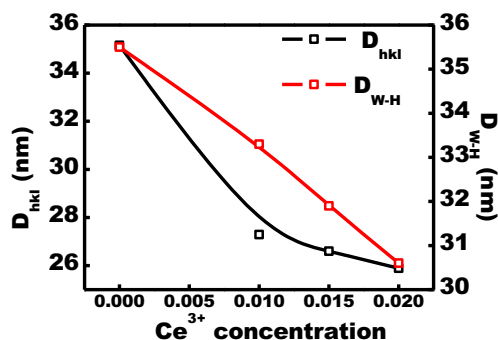
The theoretical density is determined by the following relation [26]:

$$\Delta_x = \frac{ZM}{Na^3} \qquad (5)$$

where $Z = 8$ is the number of atoms per unit cell, M is the molecular weight of the ferrite sample, N is Avogadro's number (6.023×10^{23} particles per mol) and a is the lattice parameter. As the dopant concentration increases, the lattice parameter decreases, leading to the growth of material density. The variation of the material density and the lattice parameter with dopant concentrations is shown in Fig. 4.

3.2 SEM and EDS

Figure 5 presents the SEM micrographs of the $Co_{0.5}Ni_{0.5}Fe_{2-x}Ce_xO_4$ (where $x = 0.0, 0.01, 0.015$ and 0.02) nanoparticles. The micrographs reveal that the particles are alike and are agglomerated with the increase in dopant concentration. This agglomeration results in the densification of the samples, which increases the density of the material. The same result is obtained from the XRD theoretical density calculations. During the synthesis, voluminous gases escape from the material, creating pores in the synthesized material. But, in the present study, no such evidence has been found because the reaction is highly exothermic. A sufficiently large quantity of thermal energy is required for the grain growth during combustion process. This leads to relatively fewer pores in the synthesized material, and the dense agglomeration can be seen perfectly. Figure 6 shows the EDX spectrum for each sample of $Co_{0.5}Ni_{0.5}Ce_xFe_{2-x}O_4$ (where $x = 0.0, 0.01, 0.015$ and 0.02), where one can clearly see only the peaks of Co, Ni, Fe, Ce and O. This confirms the absence of impurities in all the samples. The Ce peak intensity increases along with the increasing value of x. The surface morphology of the sample consists of some grains with relatively homogeneous distribution with an average grain size varying from 20 to
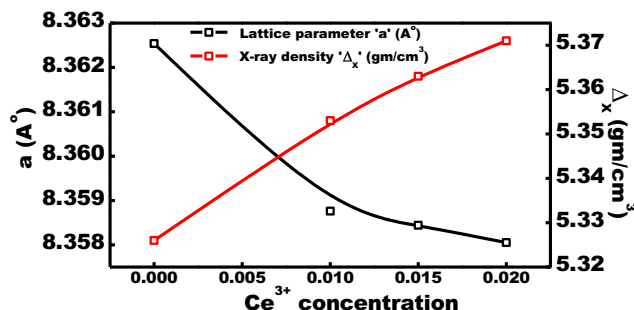

Fig. 3 Variations of crystallite size (D_{hkl}) from the Scherrer formula and of D_{W-H} from the Williamson-Hall plot with Ce^{3+} concentration

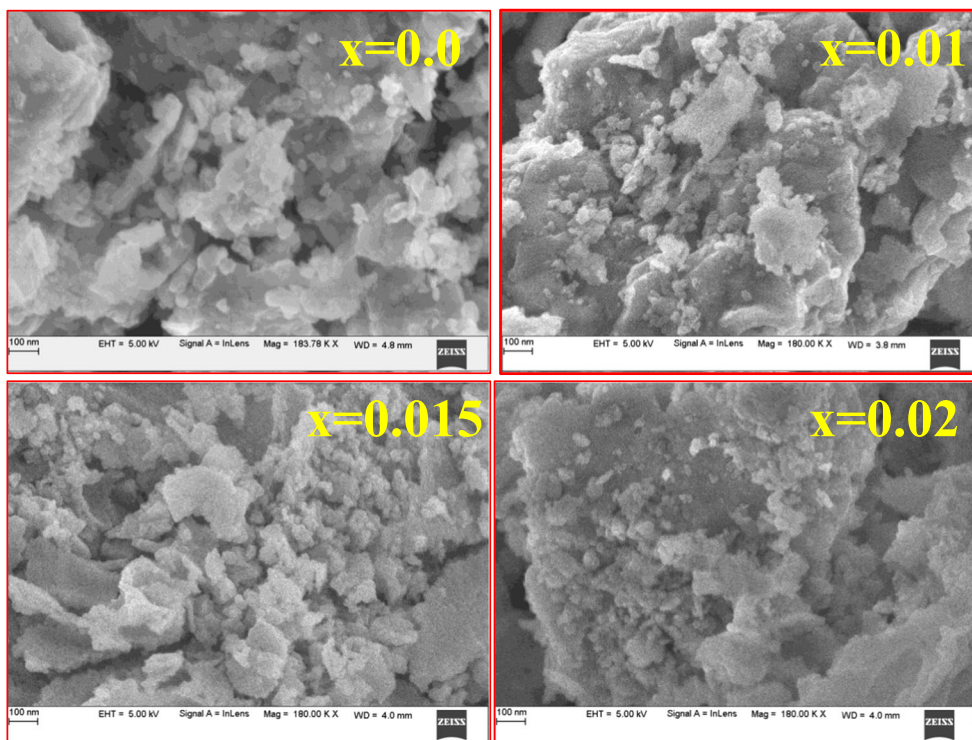**Fig. 4** Variation of lattice parameter a (in Å) and X-ray density Δ_x (in g/cm^3) with Ce^{3+} concentration

Fig. 5 SEM images of $Co_{0.5}Ni_{0.5}Fe_{2-x}Ce_xO_4$ ferrite nanoparticles with $x = 0.0, 0.01, 0.015$ and 0.02

70 nm. The nominal theoretical and experimental compositions of the samples are shown in Table 2. The estimated stoichiometry is much nearer to the anticipated values. Figure 7 shows the grain size distribution histogram. It is found that the grain size increases with the increasing Ce^{3+} concentration in the synthesized samples.

3.3 TEM

Figure 8 represents the TEM micrographs of the samples of $Co_{0.5}Ni_{0.5}Fe_{2-x}Ce_xO_4$ (where $x = 0.01, 0.015$ and 0.02). The particle size is estimated using ImageJ software, and the results of TEM images reveal that the particles appear to

Fig. 6 EDX spectra of $Co_{0.5}Ni_{0.5}Fe_{2-x}Ce_xO_4$ ferrite nanoparticles with $x = 0$ ($Co_{0.5}Ni_{0.5}Fe_2O_4$), $x = 0.01$ ($Co_{0.5}Ni_{0.5}Fe_{1.99}Ce_{0.01}O_4$), $x = 0.015$ ($Co_{0.5}Ni_{0.5}Fe_{1.985}Ce_{0.015}O_4$) and $x = 0.02$ ($Co_{0.5}Ni_{0.5}Fe_{1.98}Ce_{0.02}O_4$)

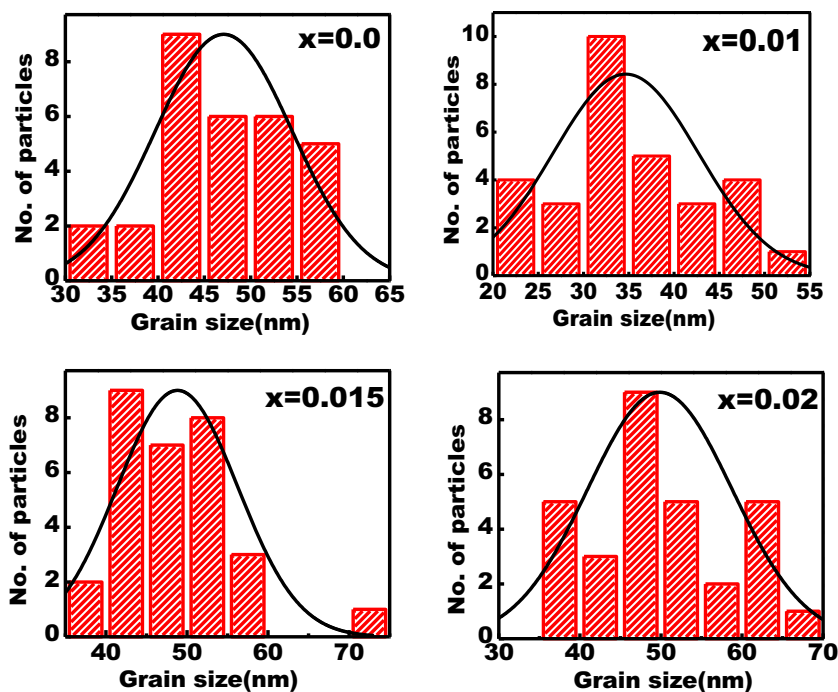**Table 2** Summary of EDX analysis of $Co_{0.5}Ni_{0.5}Fe_{2-x}Ce_xO_4$ ferrites where $x = 0.0, 0.01, 0.015$ and 0.02

Ce^{3+} concentration (x)	Elements	Composition theoretical values	Composition from EDX analysis
0	Co	0.5	0.546
	Ni	0.5	0.454
	Fe	2.0	2
	Ce	0.0	0
0.01	Co	0.5	0.575
	Ni	0.5	0.425
	Fe	1.99	1.989
	Ce	0.01	0.011
0.015	Co	0.5	0.549
	Ni	0.5	0.451
	Fe	1.985	1.984
	Ce	0.015	0.016
0.02	Co	0.5	0.562
	Ni	0.5	0.437
	Fe	1.98	1.981
	Ce	0.02	0.019

be spherical in shape and homogeneously dispersed within the crystallite size of approximately 25 to 80 nm. It should be noted that some of the particles can be seen in the

shape of elongated cuboids. Some moderately agglomerated particles as well as separated particles are also seen in the TEM micrographs. For particle size estimation, only separated particles are considered and these results are in good agreement with the XRD results. The particle size distribution histograms are shown in Fig. 8. The SAED analysis of some selected compositions is presented in the inset of TEM micrographs shown in Fig. 8, and the data for the sample with $x = 0.0$ are presented in our previous report [26]. The ring patterns do not show any additional diffraction spots resulting from the other metal oxides. The position and intensities of lines in the diffraction pattern confirm the spinel cubic structure. This characteristic feature from the SAED analysis indicates that the synthesized samples are crystalline in nature [27].

3.4 Mössbauer Spectroscopy

The experimental spectra are fitted using SpectrRelax software [28]. The isomer shifts are calculated with respect to the metallic α-Fe. The room-temperature Mössbauer spectra of $Co_{0.5}Ni_{0.5}Fe_{2-x}Ce_xO_4$ ($x = 0.0, 0.01, 0.015$ and 0.02) nanoparticles are shown in Fig. 9. The spectra consist of broadened Zeeman lines and quadrupole-split lines. The simultaneous presence of a magnetic sextet and a doublet component on the Mössbauer spectra is typical of
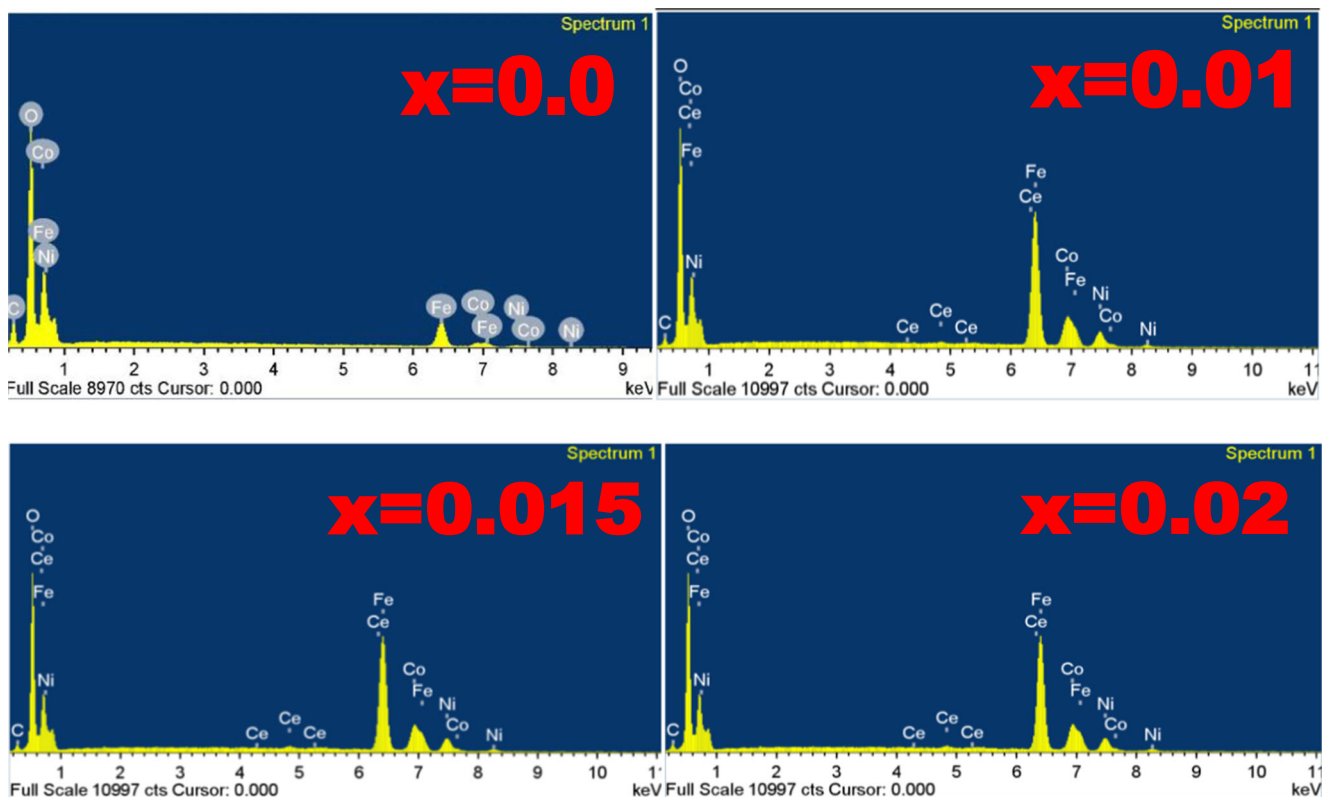

Fig. 7 Grain size distribution histogram of $Co_{0.5}Ni_{0.5}Fe_{2-x}Ce_xO_4$ ferrite nanoparticles with $x = 0.0$ ($Co_{0.5}Ni_{0.5}Fe_2O_4$), $x = 0.01$ ($Co_{0.5}Ni_{0.5}Fe_{1.99}Ce_{0.01}O_4$), $x = 0.015$ ($Co_{0.5}Ni_{0.5}Fe_{1.985}Ce_{0.015}O_4$) and $x = 0.02$ ($Co_{0.5}Ni_{0.5}Fe_{1.98}Ce_{0.02}O_4$)

Fig. 8 TEM micrographs, SAED and particle distribution diagram of $Co_{0.5}Ni_{0.5}Fe_{2-x}Ce_xO_4$ ferrite nanoparticles with $x = 0.0$ ($Co_{0.5}Ni_{0.5}Fe_2O_4$), $x = 0.01$ ($Co_{0.5}Ni_{0.5}Fe_{1.99}Ce_{0.01}O_4$), $x = 0.015$ ($Co_{0.5}Ni_{0.5}Fe_{1.985}Ce_{0.015}O_4$) and $x = 0.02$ ($Co_{0.5}Ni_{0.5}Fe_{1.98}Ce_{0.02}O_4$)
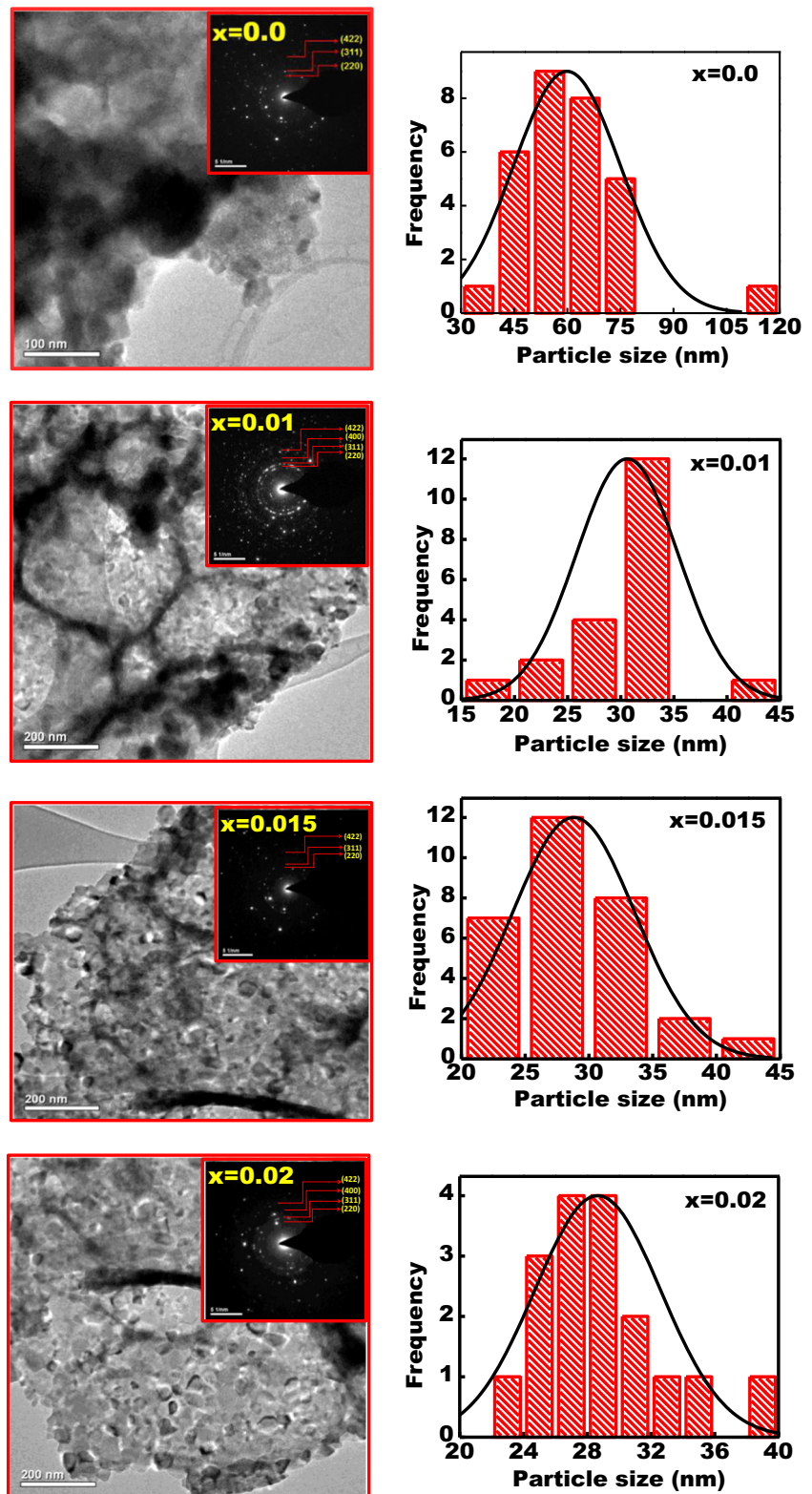
superparamagnetic nanopowder [29]. The reason of the doublet lines being present on the spectra obtained at lower temperatures than magnetic phase transition temperature is the superparamagnetic relaxation. It leads to the collapse of

Zeeman lines because the Mössbauer spectroscopy measuring time (τ_m) is much shorter than superparamagnetic relaxation time (τ_s) [30]. The temperature, at which the areas of doublet and Zeeman lines are equal, is called the blocking
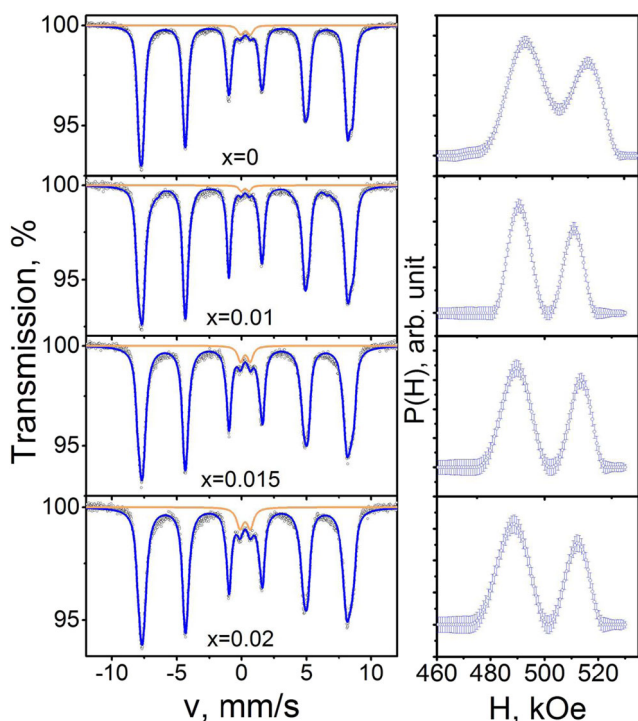
Fig. 9 Room-temperature Mössbauer spectra of $Co_{0.5}Ni_{0.5}Fe_{2-x}Ce_xO_4$ ferrite nanoparticles with $x = 0$ ($Co_{0.5}Ni_{0.5}Fe_2O_4$), $x = 0.01$ ($Co_{0.5}Ni_{0.5}Fe_{1.99}Ce_{0.01}O_4$), $x = 0.015$ ($Co_{0.5}Ni_{0.5}Fe_{1.985}Ce_{0.015}O_4$) and $x = 0.02$ ($Co_{0.5}Ni_{0.5}Fe_{1.98}Ce_{0.02}O_4$)

temperature (T_B). The T_B value depends on a particle size [31]. The decrease in particle sizes leads to the reduction of T_B. The doublet area values of $Co_{0.5}Ni_{0.5}Fe_{2-x}Ce_xO_4$ Mössbauer spectra are $\approx 3\%$ for $x = 0.0$ and $x = 0.01$, $\approx 4\%$ for $x = 0.015$ and $\approx 6\%$ for $x = 0.02$. These values indicate that T_B is higher than the room temperature, and the size of particles for the samples with $x = 0$ and

0.01 as well as $x = 0.015$ and 0.02 is close to each other, which is in good agreement with the XRD particle size data. The hyperfine magnetic field distribution functions $P(H)$ of $Co_{0.5}Ni_{0.5}Fe_{2-x}Ce_xO_4$ Mössbauer spectra (Fig. 9) have two local maxima. Each maximum corresponds to a Zeeman sextet with parameters listed in Table 3. The isomer shift of S1 sextet is 0.28 mm/s and attributed to Fe^{3+} in tetrahedron. The isomer shift of S2 sextet is 0.36 mm/s and associated with Fe^{3+} in octahedron [31].

The superparamagnetic relaxation leads to an asymmetric shape of the lines on the Mössbauer spectra with sharp outer and smeared inward sides [32]. This complicates the model interpretation and reduces the reliability of the Mössbauer spectrum parameters. To minimize the effect of paramagnetic relaxation, the low-temperature Mössbauer study is carried out. Figure 10 shows the Mössbauer spectra of $Co_{0.5}Ni_{0.5}Fe_{2-x}Ce_xO_4$ ($x = 0$–0.02) nanoparticles taken at 15 K. The $P(H)$ functions of $Co_{0.5}Ni_{0.5}Fe_{2-x}Ce_xO_4$ Mössbauer spectra have three local maxima. These maxima correspond to the three Zeeman sextets with the parameters listed in Table 4. The isomer shift value of sextet S1 is ≈ 0.37 mm/s and corresponds to Fe^{3+} state in the tetrahedron oxygen environment [31–33]. The isomer shifts of S2 and S3 sextets are ≈ 0.49 mm/s and correspond to Fe^{3+} in oxygen octahedron. Thus, the Fe^{3+} ions occupy both A and B sites. The Fe^{3+} in the B site has two types of local symmetry. The presence of three inequivalent states of Fe^{3+} ions results from cation distribution. The $P(H)$ functions of Mössbauer spectra taken at 15 K possess two maxima corresponding to octahedron sites, while at room temperature, the $P(H)$ functions have only one octahedron maximum. It appears that the decreasing temperature leads to the reduction of the superparamagnetic relaxation effect on Mössbauer spectra and the narrowing of spectrum

Table 3 Parameters of room-temperature Mössbauer spectra of $Co_{0.5}Ni_{0.5}Fe_{2-x}Ce_xO_4$ ferrites where $x = 0.0$, 0.01, 0.015 and 0.02 at low temperature (15 K)

x	Component	$\delta \pm 0.02$ (mm/s)	$\varepsilon/\Delta \pm 0.002$ (mm/s)	$H \pm 0.5$ (kOe)	$G \pm 0.02$ (mm/s)	$A \pm 1$ (%)
0	D	0.30	0.802		0.66	3
	S1	0.28	-0.002	490	0.48	53
	S2	0.36	-0.007	513	0.52	44
0.01	D	0.30	0.688		0.52	1
	S1	0.27	-0.002	490	0.62	52
	S2	0.36	-0.007	513	0.62	47
0.015	D	0.29	0.804		0.58	4
	S1	0.28	-0.002	490	0.57	54
	S2	0.36	-0.008	514	0.57	42
0.02	D	0.29	0.820		0.63	6
	S1	0.28	-0.002	487	0.57	53
	S2	0.35	-0.008	513	0.57	41

δ isomer shift, ε quadrupole splitting, Δ quadrupole splitting of paramagnetic components, H_{eff} magnetic field on ^{57}Fe nucleus, G spectral line width, A spectral component area
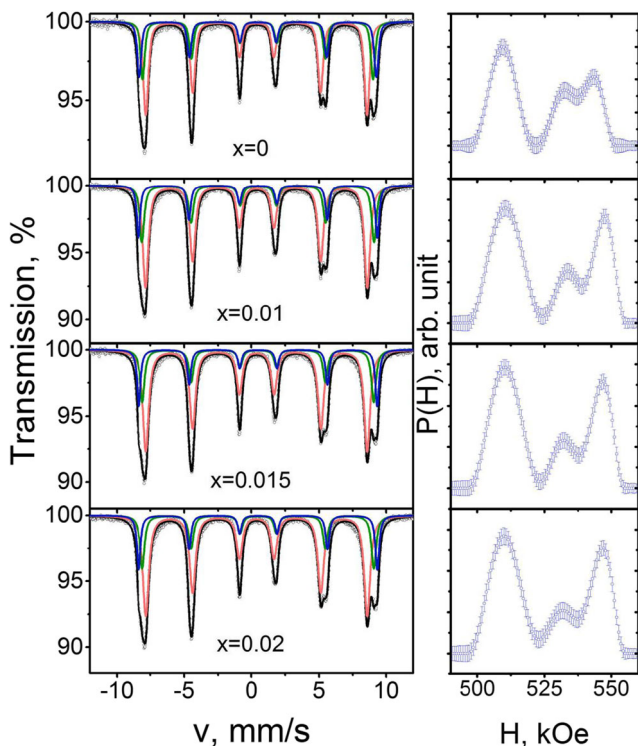
Fig. 10 Low-temperature (15 K) Mössbauer spectra of $Co_{0.5}Ni_{0.5}Fe_{2-x}$ Ce_xO_4 ferrite nanoparticles with $x = 0$ ($Co_{0.5}Ni_{0.5}Fe_2O_4$), $x = 0.01$ ($Co_{0.5}Ni_{0.5}Fe_{1.99}Ce_{0.01}O_4$), $x = 0.015$ ($Co_{0.5}Ni_{0.5}Fe_{1.985}Ce_{0.015}O_4$) and $x = 0.02$ ($Co_{0.5}Ni_{0.5}Fe_{1.98}Ce_{0.02}O_4$)

Fig. 11 Room-temperature M-H loop of $Co_{0.5}Ni_{0.5}Fe_{2-x}Ce_xO_4$ ferrite nanoparticles with $x = 0.0, 0.01, 0.015$ and 0.02

lines. This allows one to resolve the two maxima on $P(H)$ functions at 15 K, instead of one.

The value of sextet areas is approximately equal to the Fe^{3+} concentration in the occupied states. According to the data in Table 4, the area values of sextet S1 are increasing with x. Therefore, the substitutions of Fe^{3+}
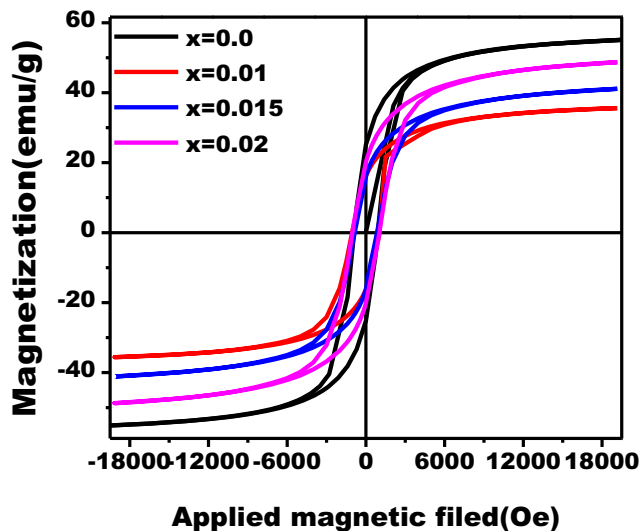
ions by Ce^{3+} lead to the cation redistribution in the $Co_{0.5}Ni_{0.5}Fe_{2-x}Ce_xO_4$ ($x = 0$–0.02) nanoparticles.

3.5 Magnetic Study

The variation of magnetization (M, emu/g) with applied magnetic field (H, kOe) for $Co_{0.5}Ni_{0.5}Fe_{2-x}Ce_xO_4$ (where $x = 0.0, 0.01, 0.015$ and 0.02) at room temperature is shown in Fig. 11. The magnetization curves demonstrate the change in magnetic behaviour of $Co_{0.5}Ni_{0.5}Fe_2O_4$ with the Ce^{3+} doping. The value of saturation magnetization (M_s), remanence (M_r), reduced remanence (R, M_r/M_s), coercivity (H_c), anisotropy constant (K_C) and magneton number (η_B) values for doped and undoped $Co_{0.5}Ni_{0.5}Fe_2O_4$ ferrites

Table 4 Parameters of Mössbauer spectra of $Co_{0.5}Ni_{0.5}Fe_{2-x}Ce_xO_4$ ferrites where $x = 0.0, 0.01, 0.015$ and 0.02 at low temperature (15 K)

x	Component	$\delta \pm 0.02$ (mm/s)	$\varepsilon \pm 0.002$ (mm/s)	$H \pm 0.5$ (kOe)	$G \pm 0.02$ (mm/s)	$A \pm 1$ (%)
0	S1	0.37	0.001	507	0.45	51
	S2	0.49	-0.012	535	0.38	25
	S3	0.47	-0.002	542	0.38	24
0.01	S1	0.37	0.001	508	0.46	53
	S2	0.49	-0.017	537	0.40	24
	S3	0.48	-0.003	547	0.35	23
0.015	S1	0.37	0.002	509	0.49	57
	S2	0.50	-0.012	533	0.41	24
	S3	0.48	-0.002	548	0.34	20
0.02	S1	0.38	0.001	508	0.50	58
	S2	0.50	-0.010	536	0.41	22
	S3	0.48	-0.001	547	0.33	20

δ isomer shift, ε quadrupole splitting, H_{eff} magnetic field on ^{57}Fe nucleus, G spectral line width, A spectral component area

Table 5 Room-temperature magnetic parameters of $Co_{0.5}Ni_{0.5}Fe_{2-x}Ce_xO_4$ ferrites where x = 0.0, 0.01, 0.015 and 0.02, i.e. saturation magnetization (M_s), remanence (M_r), reduced remanence (R), coercivity (H_c), anisotropy constant (K_C) and magneton number (η_B)

Ce³⁺ concentration (x)	M_s (emu/g)	M_r (emu/g)	$R = M_r/M_s$	H_c (Oe)	K_C (erg/cm³)	η_B (μ_B)
0.00	57.9	25.2	0.387	851	0.033	2.43
0.01	35.6	16.2	0.413	911	0.023	1.55
0.015	41.1	15.9	0.435	1030	0.022	1.74
0.02	48.7	20.1	0.455	1039	0.031	2.06

were calculated from the M-H loops [34]. These values are tabulated in Table 5. Initially, the value of M_s is decreased from 57.9 to 35.6 emu/g with the Ce³⁺ doping level for 0.01 and is then increased to 48.7 emu/g with x = 0.02. This can be explained by the fact that the ferrites follow Neel's two-sub-lattice model [35]. According to Neel's two-sub-lattice model, the magnetic moment per formula unit is given by $\eta_B = M_B - M_A$, where M_B and M_A are the B and A sub-lattice magnetic moments (in μ_B). Neel's magnetic moments are calculated by taking the ionic magnetic moment of Co²⁺, Ni²⁺, Fe³⁺ and Ce³⁺. The magnetization depends on the cation distribution in the A and B sites. The value of M_s is decreased with increasing Ce³⁺ concentration. This is due to the added paramagnetic Ce³⁺ which preferred the octahedral (B) site by displacing Fe³⁺ from the B site to the A site by diluting the magnetic moment of the B site. The net magnetization, being different between the B and A sub-lattices, is increased due to an increase in Fe³⁺ at the B site. When substitution of Ce³⁺ is increased, this prefers both the A and B sites and there may be less migration of Fe³⁺ from the A site to the B site, which eventually decreases the magnetic moment of B site and thereby M_s. This may be the main reason for the decreased magnetization for $x \geq 0.01$.

The H_c value is increased with increasing the cerium concentration, and this mainly depends upon the size of the crystallite or particle and the anisotropy of the crystal structure. The increasing H_c value suggests that the material transforms to soft magnetic nature to hard magnetic nature and this behaviour of the samples indicates that Ce-doped Co-Ni ferrites are helpful for permanent magnet applications. Remanence ratio (R) is the characteristic parameter of the magnetic materials. High R value is needed for magnetic recording and memory devices; moreover, R provides information by which the direction of magnetization reorients to the nearest easy-axis magnetization direction after the magnetic field is switched off. The varying values of R, in the present case, are an indication of the anisotropic nature of $Co_{0.5}Ni_{0.5}Fe_{2-x}Ce_xO_4$. It is observed that the values of R are in the range of 0.385 to 0.455, showing an increasing trend with Ce³⁺ doping (Table 5).

4 Conclusion

For the first time, nanocrystalline $Co_{0.5}Ni_{0.5}Fe_{2-x}Ce_xO_4$ (x = 0.0, 0.01, 0.015 and 0.02) ferrites have been synthesized successfully by the modified solution combustion method using a mixture of carbamide and glucose as fuels. The impact of larger rare-earth Ce³⁺ on the structural, microstructural and low-temperature Mössbauer spectroscopy of the ferrite samples has been thoroughly investigated. The XRD results reveal that the synthesized samples are monophasic without any additional impurity pickup, and the XRD patterns exhibit spinel cubic structure. The crystallite size decreases with the addition of Ce³⁺ content to the host ferrite, which is in good agreement with the crystallite size obtained from TEM micrographs and Williamson-Hall plots. The declining trend of lattice parameter is observed due to the fact that larger ionic radii of rare-earth ions at Fe³⁺ site induce lattice distortion and internal strain. The increased internal strain results to lesser arrangement of Ce³⁺–O²⁻ bonds which leads to larger crystalline anisotropy. The SEM micrographs reveal that particles are alike and are agglomerated with the increased dopant concentration. The EDS results confirm the stoichiometry much nearer to the anticipated values. The room-temperature Mössbauer spectra exhibit magnetic sextet and doublet components simultaneously, which suggests that the synthesized material is a superparamagnetic nanopowder. The doublet area increases by adding Ce³⁺ to the ferrite sample. It can be concluded that the blocking temperature is above room temperature. The low-temperature Mössbauer spectra have three Zeeman sextets. The isomer shift values of the sextets indicate that Fe³⁺ ions exist in both tetrahedral and octahedral environments. The growth of the sextet area corresponding to Fe³⁺ tetrahedral site is the evidence of the substitution of Fe³⁺ by Ce³⁺ at the octahedral sites. With the small value of Ce³⁺ doping, the saturation magnetization values are decreased initially and then increased. Further, the value of coercivity is found to be increasing with increasing Ce³⁺ concentration. These results corroborate a favourable change in the magnetic behaviour of $Co_{0.5}Ni_{0.5}Fe_2O_4$ when doped with Ce³⁺ in different proportions, and these ferrites can have potential

for magnetic recording, memory devices and permanent magnet applications.

References

1. Sanchez-Marcos, J., Mazario, E., Rodriguez-Velamazan, J.A., Salas, E., Herrasti, P., Menendez, N.: Cation distribution of cobalt ferrite electrosynthesized nanoparticles. A methodological comparison. J. Alloy. Compd. **739**, 909–917 (2018)

2. Zalnėravicius, R., Paskevicius, A., Mazeika, K., Jagminas, A.: Fe(II)-substituted cobalt ferrite nanoparticles against multidrug resistant microorganisms. Appl. Surf. Sci. **435**, 141–148 (2018)

3. Kumar, L., Kumar, P., Kuncser, V., Greculeasa, S., Sahoo, B., Kar, M.: Strain induced magnetism and superexchange interaction in Cr substituted nanocrystalline cobalt ferrite. Mater. Chem. Phys. **211**, 54–64 (2018)

4. Motavallian, P., Abasht, B., Abdollah-Pour, H.: Zr doping dependence of structural and magnetic properties of cobalt ferrite synthesized by sol-gel based Pechini method. J. Magn. Magn. Mater. **451**, 577–586 (2018)

5. Barrera, G., Coisson, M., Celegato, F., Raghuvanshi, S., Mazaleyrat, F., Kane, S.N., Tiberto, P.: Cation distribution effect on static and dynamic magnetic properties of $Co_{1-x}Zn_xFe_2O_4$ ferrite powders. J. Magn. Magn. Mater. **456**, 372–380 (2018)

6. Song, N., Gu, S., Wu, Q., Li, C., Zhou, J., Zhang, P., Wang, W., Yue, M.: Facile synthesis and high-frequency performance of $CoFe_2O_4$ nanocubes with different size. J. Magn. Magn. Mater. **456**, 793–798 (2018)

7. Lyubutin, I.S., Starchikov, S.S., Baskakov, A.O., Gervits, N.E., Lin, C.-R., Tseng, Y.-T., Lee, W.-J., Shih, K.-Y.: Exchange-coupling of hard and soft magnetic sublattices and magnetic anomalies in mixed spinel $NiFe_{0.75}Cr_{1.25}O_4$ nanoparticles. J. Magn. Magn. Mater. **451**, 336–343 (2017)

8. Mondal, R., Dey, S., Sarkar, K., Dasgupta, P., Kumar, S.: Influence of high energy ball milling on structural parameters, cation distribution and magnetic enhancement of nanosized $Co_{0.3}Zn_{0.7}Fe_2O_4$. Mater. Res. Bull. **102**, 160–171 (2018)

9. Sharmaa, R., Komal, Kumar, V., Bansal, S., Singhal, S.: Boosting the catalytic performance of pristine CoFe2O4 with yttrium (Y^{3+}) inclusion in the spinel structure. Mater. Res. Bull. **90**, 94–103 (2017)

10. Humbe, A.V., Kounsalye, J.S., Shisode, M.V., Jadhav, K.M.: Rietveld refinement, morphology and superparamagnetic of nanocrystalline $Ni_{0.70-x}Cu_xZn_{0.30}Fe_2O_4$ spinel ferrite. Ceram. Int. **44**, 5466–5472 (2018)

11. Gore, S.K., Mane, R.S., Naushad, Mu., Jadhav, S.S., Zate, M.K., Alothman, Z.A., Hui, B.K.N.: Influence of Bi^{3+}-doping on the magnetic and Mössbauer properties of spinel cobalt ferrite. Dalton Trans. **44**, 6384–6390 (2015)

12. Gawas, S.G., Meena, S.S., Yusuf, S.M., Verenkar, V.M.S.: Anisotropy and domain state dependent enhancement of single domain ferrimagnetism in cobalt substituted Ni-Zn ferrites. New J. Chem. **40**, 9275–9284 (2016)

13. Nordhei, C., Lund Ramstad, A., Nicholson, D.G.: Nanophase cobalt, nickel and zinc ferrites: synchrotron XAS study on the crystallite size dependence of metal distribution. Phys. Chem. Chem. Phys. **10**, 1053–1066 (2008)

14. Kumar, G., Kotnala, R.K., Shah, J., Kumar, V., Kumar, A., Singh, P.D.M.: Cation distribution: a key to ascertain the magnetic interactions in a cobalt substituted Mg–Mn nanoferrite matrix. Phys. Chem. Chem. Phys. **19**, 16669–16680 (2017)

15. Fayek, M.K., Bahgat, A.A.: Fe^{57} Mossbauer study in cobalt substituted magnetite. Z. Phys. B-Condens. Matter **46**, 199–205 (1982)

16. Ndlovu, B., Msomi, J.Z., Moyo, T.: Mössbauer and electrical studies of $Ni_xCo_{1-x}Fe_2O_4$ nanoparticles. J. Alloys Compd. **749**, 672–680 (2018)

17. Nikumbh, A.K., Nagawade, A.V., Tadke, V.B., Bakare, P.P.: Electrical, magnetic and Mossbauer properties of cadmium - cobalt ferrites prepared by the tartarate precursor method. J. Mater. Sci. **36**, 653–662 (2001)

18. Rao, G.S.N., Caltun, O.F., Rao, K.H., Parvatheeswara Rao, B., Ajay Gupta, S.N.R., Rao, A., Kumar, M.: Mössbauer and magnetic study of silicon substituted cobalt ferrite. Hyperfine Interact. **184**, 51–55 (2008)

19. Rusanov, V., Gushterov, V., Nikolov, S., Trautwein, A.X.: Detailed Mössbauer study of the cation distribution in $CoFe_2O_4$ ferrites. Hyperfine Interact. **191**, 67–74 (2009)

20. Chauhan, L., Singh, N., Dhar, A., Kumar, H., Kumar, S., Sreenivas, K.: Structural and electrical properties of Dy^{3+} substituted $NiFe_2O_4$ ceramics prepared from powders derived by combustion method. Ceram. Int. **43**, 8378–8390 (2017)

21. Tsvetkov, M., Milanova, M., Pereira, L.C.J., Waerenborgh, J.C., Cherkezova-Zheleva, Z., Zaharieva, J., Mitov, I.: Magnetic properties of binary and ternary mixed metal oxides $NiFe_2O_4$ and $Zn_{0.5}Ni_{0.5}Fe_2O_4$ doped with rare earths by sol–gel synthesis. Chem. Pap. **70**, 1600–1610 (2016)

22. Bhasker, U., Yelasani, V., Ramana, V., Musugu, R.: Structural, electrical and Magnetic characteristics of nickel substituted cobalt ferrite nano particles, synthesized by self combustion method. J. Magn. Magn. Mater. **374**, 376–380 (2015)

23. Jagadeesha Angadi, V., Rudraswamy, B., Sadhana, K., Praveena, K.: Structural and magnetic properties of manganese zinc ferrite nanoparticles prepared by solution combustion method using mixture of fuels. J. Magn. Magn. Mater. **409**, 111–115 (2016)

24. Jagadeesha Angadi, V., Rudraswamy, B., Sadhana, K., Ramana Murthy, S., Praveena, K.: Effect of Sm^{3+}-Gd^{3+} on structural, electrical and magnetic properties of Mn-Zn ferrites synthesized via combustion route. J. Alloy. Compd. **656**, 5–12 (2016)

25. Ranjith Kumar, E., Jayaprakash, R., Kumar, S.: The role of annealing temperature and bio template (egg white) on the structural, morphological and magnetic properties of manganese substituted MFe_2O_4 (M=Zn, Cu, Ni, Co) nanoparticles. J. Magn. Magn. Mater. **351**, 70–75 (2014)

26. Srinivasamurthy, K.M., Jagadeesha, A.V., Kubrin, S.P., Matteppanavar, S., Sarychev, D.A., Mohan Kumar, P., Workineh Azale, H., Rudraswamy, B.: Tuning of ferrimagnetic nature and hyperfine interaction of Ni^{2+} doped cobalt ferrite nanoparticles for power transformer applications. Accepted manuscript. Ceram. Int. https://doi.org/10.1016/j.ceramint.2018.02.129 (2018)

27. Angadi, V.J., Anupama, A.V., Kumar, R., Matteppanavar, S., Rudraswamy, B., Sahoo, B.: Observation of enhanced magnetic pinning in Sm^{3+} substituted nanocrystalline Mn–Zn ferrites prepared by propellant chemistry route. J. Alloys Compd. **682**, 263–274 (2016)

28. Matsnev, M.E., Rusakov, V.S.: SpectrRelax: an application for Mössbauer spectra modeling and fitting. AIP Conf. Proc. **1489**, 178–185 (2012)

29. Küdning, W., Bömmel, H.: Some properties of supported small α-Fe_2O_3 particles determined with the Mossbauer effect. Phys. Rev. **142**, 327–333 (1966)

30. Bodker, F., Mørup, S.: Size dependence of the properties of hematite nanoparticles. Europhys. Lett. **52**(2), 217–223 (2000)

31. Chuev, M.A.: On the shape of gamma-resonance spectra of ferrimagnetic nanoparticles under conditions of metamagnetism. JETP Lett. **98**(8), 465–470 (2013)

32. Menil, F.: Systematic trends of the ^{57}Fe Mossbauer isomer shifts in (FeO_n) and (FeF_n) polyhedra. Evidence of a new correlation between the isomer shift and the inductive effect of the competing bond T-X (*Fe) (where X is O or F and T any element with a formal positive charge). J. Phys. Chem. Solids. **46**(7), 763–789 (1985)

33. Vandenberghe, R.E., Grave, E.D.: Mossbauer effect studies of oxidic spinels. In: Long, G.J., Grandjean, F. (eds.) Mössbauer spectroscopy applied to inorganic chemistry, vol. 3, pp. 59–172. Springer Science & Business Media, New York (1989)

34. Jagdeesha Angadi, V., Choudhury, L., Sadhana, K., Liu, H.-L., Sandhya, R., Matteppanavar, S., Rudraswamy, B., Pattar, V., Anavekar, R.V., Praveena, K.: Structural, electrical and magnetic properties of Sc^{3+} doped Mn-Zn Ferrite nanoparticles. J. Magn. Magn. Mater. **424**, 1–11 (2017)

35. Jagadeesha Angadi, V., Anupama, A.V., Harish, K., Choudhary, R., Kumar, H.M., Somashekarappa, M., Mallappa, B., Rudraswamy, B.: Sahoo: Mechanism of γ-irradiation induced phase transformations in nanocrystalline $Mn_{0.5}Zn_{0.5}Fe_2O_4$ ceramics. J. Solid State Chem. **246**, 119–124 (2017)